

Measuring the Hall effect in hysteretic materials

Jaime M. Moya,¹ Anthony Voyemant,² Sudipta Chatterjee,¹ Scott B. Lee,¹ Grigorii Skorupskii,¹ Connor J. Pollak,¹ and Leslie M. Schoop^{1,*}

¹*Department of Chemistry, Princeton University, Princeton, NJ 08544, USA*

²*Department of Physics and Astronomy, California State University, Northridge, CA 91330, USA*

(Dated: December 23, 2025)

Measurement of the Hall effect is a ubiquitous probe for materials discovery, characterization, and metrology. Inherent to the Hall measurement geometry, the measured signal is often contaminated by unwanted contributions, so the data must be processed to isolate the Hall response. The standard approach invokes Onsager-Casimir reciprocity and antisymmetrizes the raw signal about zero applied magnetic field. In hysteretic materials this becomes nontrivial, since Onsager-Casimir relations apply only to microscopically reversible states. Incorrect antisymmetrization can lead to artifacts that mimic anomalous or topological Hall signatures. The situation is especially subtle when hysteresis loops are not centered at zero applied field, as in exchange-biased systems. A practical reference for generically extracting the Hall response in hysteretic materials is lacking. Here, using $\text{Co}_3\text{Sn}_2\text{S}_2$ as a bulk single-crystal model that can be prepared with or without exchange-biased hysteresis, we demonstrate two procedures that can be used to extract the Hall effect: (1) reverse-magnetic-field reciprocity and (2) antisymmetrization with respect to applied field. We then measure the Hall effect on CeCoGe_3 , a noncentrosymmetric antiferromagnet which can be prepared to have asymmetric magnetization and magnetoresistance, and demonstrate how improper processing can generate artificial anomalous Hall signals. These methods are generic and can be applied to any conductor.

I. INTRODUCTION

The Hall effect refers to the development of a transverse voltage across a material carrying current in the presence of a magnetic field via the antisymmetric component of the resistivity tensor. It provides crucial insights into charge carrier properties such as type, density, and mobility, making it a foundational tool in materials characterization. Beyond traditional applications, the Hall effect underpins key advances in spintronics [1–3], topological materials [4], and sensor technologies [5]. In the materials discovery community, measurements of the Hall effect have been extensively used in recent years to identify and/or characterize systems with reciprocal-space Berry curvature by the anomalous Hall effect (AHE) [2, 4, 6–9], real-space Berry curvature by the topological Hall effect (THE) [3, 10], and complex spin textures with non-zero scalar spin chirality (SSC) [3, 11]. With the proliferation of reports of such “exotic” Hall responses, ensuring accurate and reproducible Hall measurements has become increasingly important. However, in materials that exhibit magnetic hysteresis or complex domain behavior, extracting the true Hall signal can be nontrivial and may lead to artificial features that mimic AHE-, THE-, or SSC-like signatures.

In principle, measuring the Hall effect is straightforward. Consider a standard Hall bar geometry within a Cartesian coordinate system, where a current I_x is applied and the transverse voltage V_y is measured in the presence of a magnetic induction field $B_z = \mu_0(H_z + M_z)$, with H_z the applied field and M_z the magnetization.

Within the linear-response regime, the transverse voltage is related to the resistance tensor $R_{ij}(B_z)$ by $V_y(B_z) = I_x R_{yx}(B_z)$. R_{yx} generally contains two components: an antisymmetric (odd) Hall resistance, $R_{yx}^{odd}(+B_z) = -R_{yx}^{odd}(-B_z)$, and a symmetric (even) transverse magnetoresistance $R_{yx}^{even}(+B_z) = R_{yx}^{even}(-B_z)$. “Antisymmetric” or “symmetric” refer to the form of the matrix representing the magnetoresistance, while “odd” or “even” refer to the specific matrix element’s response to the inversion of the magnetic induction field. Symmetry constrains R_{yx} to be purely odd-in field if the measurement plane has rotational symmetry of order > 2 , or if B_z is perpendicular to an axis with even n -fold rotational symmetry and the measurement plane is aligned with that axis [12]. Therefore, trigonal, monoclinic, and triclinic crystal systems can have even-in-field R_{yx}^{even} components even when the measurement is done along a high-symmetry orientation. However, the effect can be present in higher-symmetry systems if the current, voltage and magnetic field are not all orthogonal or along principal axes depending on the point group. The point groups that allow even-in-field contributions to R_{yx} are listed by Akgöz and Saunders [13], and may also be checked via the magnetoresistance tensor on the Bilbao Crystallographic Server [14].

In practice, particularly for bulk single crystals where electrical contacts are applied manually, a voltage contact misalignment introduces an additional longitudinal voltage component $V_x = I_x R_{xx}^{even}(B_z)$ into the measured signal. The measured voltage is therefore a combination, $V_m(B_z) = I_x [R_{yx}^{odd}(B_z) + R_{yx}^{even}(B_z) + R_{xx}^{even}(B_z)]$. To extract the Hall voltage, one typically exploits the Onsager-Casimir reciprocity relations which imply that the antisymmetric components of the intrinsic mag-

* lschoop@princeton.edu

netotransport tensors, i.e., the magnetoconductivity σ and the magnetoresistivity ρ , are strictly \mathbf{B} -odd, and the symmetric components are strictly \mathbf{B} -even [13, 15–17]. Under the usual assumptions of a well-defined current path and measurement geometry, $\rho_{yx} \propto R_{yx}$ and $\rho_{xx} \propto R_{xx}$ up to geometry factors, and therefore the measured resistances inherit these symmetries. Explicitly, $R_{ij}^{even}(+B_z) = R_{ij}^{even}(-B_z)$ and $R_{ij}^{odd}(+B_z) = -R_{ij}^{odd}(-B_z)$. These relations hold for linear, microscopically reversible systems. By subtracting (antisymmetrizing) the measured voltage under B_z reversal, one cancels the B_z -even components, yielding the antisymmetric component of the tensor,

$$R_{yx}^{odd}(B_z) = \frac{R_m(+B_z) - R_m(-B_z)}{2}, \quad (1)$$

where $R_m = V_m/I_x$.

A conundrum arises because in an electrical transport measurement the following aspects are true: only H_z is controlled, M_z can be path dependent, and is it not directly measured, while Onsager-Casimir reciprocity only holds for $B_z = \mu_0(H_z + M_z)$. In materials without magnetic hysteresis, the conundrum is easily avoided, since M_z , and consequently B_z , are antisymmetric with respect to $H = 0$. Thus, the Onsager-Casimir relations also hold for H_z and

$$R_{yx}^{odd}(H_z) = \frac{R_m(+H_z) - R_m(-H_z)}{2}. \quad (2)$$

However, in materials with magnetic hysteresis including ferromagnets, antiferromagnets with complicated domains, metamagnets, glassy magnets and exchange-biased (EB) systems (hysteresis loops not centered around $H = 0$) - $M(H)$ and $R_{ij}(H)$ may be path dependent and multi-valued. In cases of magnetic hysteresis, the Onsager-Casimir reciprocity relations can still hold in principle, but only between fully time-reversed states (TRS). Experimentally, this means that to use the Onsager-Casimir relations, one must prepare the sample with time-reversed B_z , which may not correspond to equal and opposite H_z for a continuous sweep. Failing to account for this distinction can lead to systematic, reproducible artifacts that mimic THE or AHE signals.

Schematics of common THE- and AHE-like artifacts are shown in Figure 1a,b, respectively. These artifacts can arise from improper accounting for hysteresis or from trapped flux in a superconducting magnet. For hysteresis loops centered at $H = 0$, the former can be mitigated by measuring the full hysteresis loop and antisymmetrizing between TRS. However, the latter cannot always be fully eliminated, especially when the magnetoresistance is large and field-based antisymmetrization is used. If the hysteresis is not centered at $H = 0$, R_m cannot be reliably antisymmetrized using a single hysteresis loop with field-based antisymmetrization. Although methods for handling centered hysteresis are described in the

methods section of some papers [18, 19], these methods can be prone to trapped flux artifacts, and we could not find a general reference addressing non-centered hysteresis loops. Given how common and useful Hall measurements are and how easily artifacts can arise, a clear and practical reference for extracting the Hall response in hysteretic materials is still needed.

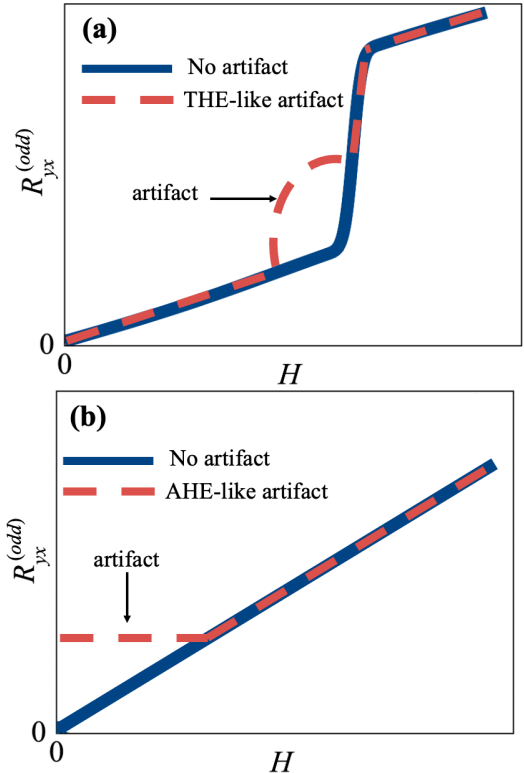


FIG. 1. Schematics of (a) topological Hall effect THE-like and (b) anomalous Hall effect AHE - like artifacts that can arise in measuring the magnetic field H dependent Hall resistance R_{yx}^{odd} . The blue lines symbolize data with no artifact, and the red dashed lines symbolize the signal contaminated with experimental artifacts. The (a) THE-like artifact shows up as an unexpected feature at finite applied magnetic field H , while the (b) AHE-like artifact gives finite R_{yx}^{odd} at $H=0$.

Particularly relevant is the advent of finding EB effects in single-crystalline conductors. Historically, EB was associated with engineered AFM/FM thin-film heterostructures [20] where lithography or related techniques are often used to create electrical contacts to minimize longitudinal contamination of the measured Hall voltage. However, EB or more generically non-centered thermodynamic or transport hysteresis loops are now more commonly reported in conductive single crystals with no engineered interfaces. For example, in $\text{Co}_3\text{Sn}_2\text{S}_2$, field training produces EB AHE hysteresis loops in a kagomé Weyl ferromagnet [21, 22]. $\text{Fe}_{1/3+\delta}\text{NbS}_2$ displays giant EB magnetization loops due to magnetic phase coexistence [23]. The layered antiferromagnetic topological insulator family $\text{MnBi}_2\text{Te}_4(\text{Bi}_2\text{Te}_3)_n$ also show field-trainable EB in their Hall response, arising from uncompensated inter-

facial spins and mixed AFM/FM character between adjacent septuple/ quintuple blocks in a single crystal, rather than a fabricated AFM/FM bilayer [24, 25]. NbMnP, a noncollinear antiferromagnet, shows an AHE effect together with asymmetric, bias-like hysteresis in magnetization [26].

In the original report of the EB AHE in $\text{Co}_3\text{Sn}_2\text{S}_2$, the extrinsic quantity, the Hall *resistance*, was reported where the longitudinal component of the measured resistance was subtracted in such a way that did not allow for reporting of the intrinsic quantity, the Hall *resistivity*, due to the fact that the magnetic hysteresis is by definition not centered around $H = 0$ [21]. In determining the origins of AHE, the intrinsic magnitude of the Hall conductivity (and thereby the Hall resistivity) is an essential quantity since it can be compared directly with theoretical calculations. Furthermore, the methods used in that report take advantage of the fact that the Hall voltage is exceptionally large in $\text{Co}_3\text{Sn}_2\text{S}_2$, which is not generally true for most magnetic materials. This further creates a clear impetus to establish generic procedures for extracting the Hall response in systems that show non-centered hysteresis loops.

Here, we present methods for processing Hall effect data in magnetically hysteretic materials using (1) the reverse-magnetic-field reciprocity (RMFR) method [27] and (2) antisymmetrization with respect to H_z between TRS. These methods are general and can also be applied to non-magnetic materials. The RMFR method, derived only assuming the Onsager form of the magnetotransport tensors, relies on interchanging current and voltage sources, was originally developed for non-magnetic materials [27], while we verify it is valid and particularly useful in hysteretic magnetic materials. On the other hand, antisymmetrization, which relies on reversing the applied magnetic field, is commonly used, but sometimes misapplied, leading to artifacts that mimic the AHE or THE. We benchmark these methods on $\text{Co}_3\text{Sn}_2\text{S}_2$, which can be prepared either with or without an EB hysteresis, using a generic decision tree we provide that can be used to minimize artifacts in Hall measurements. We show that both methods remain valid even when the magnetic hysteresis loops are not symmetric about $H = 0$, provided that the data processing uses TRS.

The main advantages of the RMFR method are three-fold: (1) for a given H - T history it yields twice as much independent Hall data and is therefore twice as time-efficient as antisymmetrization, (2) it mitigates artifacts from trapped flux, and (3) its procedure is independent of whether hysteresis is present. In contrast, antisymmetrization is useful when only one source/measure channel is available, whereas RMFR requires either two source/measure channels or a switch box. However, as we will demonstrate, the antisymmetrization procedure depends on the type of hysteresis and can suffer from artifacts due to trapped flux.

We also use measurements on CeCoGe_3 [28, 29], a system we show can be prepared with asymmetric magne-

tization and resistivity via specific field-cooling procedures, to demonstrate how incorrect antisymmetrization can produce artifacts that mimic the spontaneous AHE. We conclude by discussing how to identify and correct artifacts in Hall data, outlining practical considerations for contact geometry, and highlighting a class of materials where these methods should be especially valuable.

II. THE TEST CASE: $\text{Co}_3\text{Sn}_2\text{S}_2$

$\text{Co}_3\text{Sn}_2\text{S}_2$, a Shandite compound crystallizing in the $R3\bar{m}$ space group that orders ferromagnetically near $T_C \sim 175$ K [30–33], is an ideal platform to test measuring the AHE in cases where the magnetic hysteresis is or is not centered about $H = 0$. With application of $H \parallel c$, a large AHE is registered below T_C which was linked to Weyl fermions in its Fermi surface [34, 35]. A second anomaly was observed in various measurements near $T_A \sim 125$ K [21, 36–39] with its origins debated [38, 40–43]. Below T_A , magnetic memory effects are observed [43], including an EB AHE which can be achieved by field cooling the sample from above T_C through T_A likely due to magnetic phase coexistence [21, 22].

We have grown single crystals of $\text{Co}_3\text{Sn}_2\text{S}_2$ out of a ternary melt described in Methods. The crystal structure was checked using X-ray diffraction (Figure S1, Tables S1-4) and refinements are consistent with previous reports. In Figure 2a-c we present H -dependent isothermal magnetization M (blue, left axis) and longitudinal resistivity ρ_{xx} (pink, right axis) measured on $\text{Co}_3\text{Sn}_2\text{S}_2$ at temperature $T = 5$ K with $H \parallel c$ under various field cooling procedures.

The field cooling procedures are shown schematically in Figure 3a,b. Explicitly, for the ZFC case, the crystal was cooled in the absence of H from $T_{max} = 300$ K to $T_{meas} = 5$ K. H was then ramped from $0 \rightarrow +1$ T $\rightarrow -1$ T $\rightarrow 1$ T. Here, no EB behavior is observed as the hysteresis loops are centered around $H = 0$ in M and ρ_{xx} (Figure 2a). To induce the EB effect, the sample was field cooled at $\mu_0 H_{FC} = +1$ T from 300 K then a hysteresis loop was measured at $T = 5$ K from $+1$ T $\rightarrow -1$ T $\rightarrow 1$ T, schematically shown in Figure 3b as the positive FC procedure. The corresponding procedure for $\mu_0 H_{FC} = -1$ T is labeled as the negative FC procedure in Figure 3b where the field cooling procedure was the same but the field cooling and field sweep protocol was reversed i.e the sample was field cooled in $\mu_0 H_{FC} = -1$ T from 300 K and the hysteresis loops were measured from -1 T $\rightarrow 1$ T $\rightarrow -1$ T. The EB effect is observed as a bias of the M and ρ_{xx} hysteresis loops towards the left of $H = 0$ for $\mu_0 H_{FC} = +1$ T (Figure 2b) and to the right for $\mu_0 H_{FC} = -1$ T (Figure 2c) consistent with previous measurements [21]. In all three of these cases there are regions where $M(H) \neq -M(-H)$, and therefore Eq. 2 cannot be used to antisymmetrize the Hall data. In the following, we describe two methods to extract the Hall effect and demonstrate them on $\text{Co}_3\text{Sn}_2\text{S}_2$.

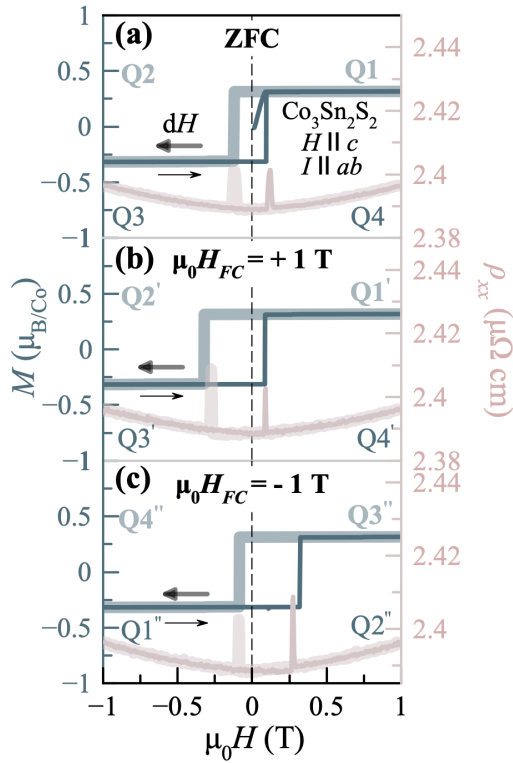


FIG. 2. Isothermal magnetization (M) (blue, left axis) and longitudinal resistivity (ρ_{xx}) (pink, right axis) measured on $\text{Co}_3\text{Sn}_2\text{S}_2$ at $T = 5$ K after cooling the sample from 300 K using the (a) zero-field cooled (ZFC) protocol, (b) positive field cool protocol with $\mu_0 H_{FC} = +1$ T and (c) negative field cool protocol with $\mu_0 H_{FC} = -1$ T. For the ZFC protocol in (a), the sample was cooled in zero field from $T_{max} = 300$ K to $T_{meas} = 5$ K, then the magnetic field was swept $0 \rightarrow +1$ T $\rightarrow -1$ T $\rightarrow +1$ T. For the positive field-cool protocol in (b), the sample was cooled from T_{max} to T_{meas} in $\mu_0 H_{FC} = +1$ T, and the field was swept $+1$ T $\rightarrow -1$ T $\rightarrow +1$ T. For the negative field-cool protocol in (c), the sample was cooled from T_{max} to T_{meas} in $\mu_0 H_{FC} = -1$ T, and the field was swept -1 T $\rightarrow +1$ T $\rightarrow -1$ T. Q1-Q4 label the sequential quarter-segments of the field sweep; for the (a) ZFC loop these correspond to $+1$ T $\rightarrow 0$, $0 \rightarrow -1$ T, -1 T $\rightarrow 0$, and $0 \rightarrow +1$ T, respectively. Q1'-Q4' denote the analogous segments for the (b) positive field-cool protocol, while Q1''-Q4'' in (c) sequentially correspond to -1 T $\rightarrow 0$, $0 \rightarrow 1$ T, 1 T $\rightarrow 0$, and $0 \rightarrow -1$ T (c) for the negative field-cool protocol. All measurements were performed with the applied magnetic field $H \parallel c$ while the transport measurements were performed with the current $I \parallel ab$.

III. METHODS FOR EXTRACTING THE HALL EFFECT

We first introduce the RMFR and antisymmetrization methods. Schematics of two measurements, labeled m1 (blue) and m2 (red) are shown in Figure 3c, where the current and voltage contacts are interchanged relative to each other. Physically, the RMFR method [27] follows

from Onsager-Casimir reciprocity of the magnetotransport tensors. For a linear, ohmic conductor this implies that in a four-terminal resistance device, the voltage pattern produced by driving current from contact 1 to 2 in field $+B_z$ (Figure 3c (m1, blue)) is identical to that produced by driving the same current from 3 to 4 in $-B_z$ (Figure 3c (m2, red)) with the roles of current and voltage contacts interchanged. Thus, interchanging current and voltage leads at fixed B_z is equivalent to keeping the leads fixed and reversing the magnetic induction field ($+B_z \rightarrow -B_z$). Therefore, measurements m1(blue) and m2(red) are time-reversed state equivalents. Since rotating the electrical contacts equivalently reverses the polarity of B for any H , Eq. 2 can be re-written as

$$R_{yx}^{odd}(H_z) = \frac{R_{m1}(H_z) - R_{m2}(H_z)}{2}. \quad (3)$$

This procedure assumes that appropriate averaging techniques are used to eliminate thermoelectric voltages. In a direct current (DC) transport measurement, this can be achieved by reversing the current and appropriately averaging such that $R_{m1} = \frac{R_{12,34} - R_{21,34}}{2}$ and $R_{m2} = \frac{R_{34,12} - R_{43,12}}{2}$, where the first indices represent the current source and drain contacts, and the second indices represent the high and low limit voltage contacts [44].

Instead, we adopt the common practice of using low-frequency alternating current (AC) lock-in transport measurements to eliminate thermoelectric voltages and approximate the DC limit reducing the procedure to two measurements with $R_{m1} = R_{12,34}$ and $R_{m2} = R_{34,12}$. Furthermore, the AC lock-in technique allows for simultaneous acquisition of R_{m1} and R_{m2} if two AC current sources and voltage measure modules are available and appropriate lock-in and grounding techniques are considered. The techniques we used for simultaneous acquisition of R_{m1} and R_{m2} are described in Methods.

In general, the only constraints of the RMFR method are that the device under test be ohmic (the current-voltage relationship is linear, which we have checked in our devices), and the states at $+B_z$ and $-B_z$ are time-reversed counterparts (i.e. the Onsager-Casimir relations hold) [27]. While we have shown m1 (blue) and m2 (red) in Figure 3c for a Van der Pauw (VdP) geometry, Hall bar or other more arbitrary geometries can also work for the RMFR method [45]. It goes without saying that the same exact contacts should be used for both measurements. So long as these conditions are met and R_{m1} and R_{m2} are taken simultaneously or sequentially (if simultaneous acquisition is not possible) without changing H , the RMFR method together with Eq. 3 can be used to extract the Hall effect for an arbitrary $H - T$ history.

This is in stark contrast to isolating Hall signals by antisymmetrizing with respect to H . Here we will refer to this process as “antisymmetrization.” The idea is that two measurements m1 and m1' are taken with the same contact geometry at equal and opposite H , as

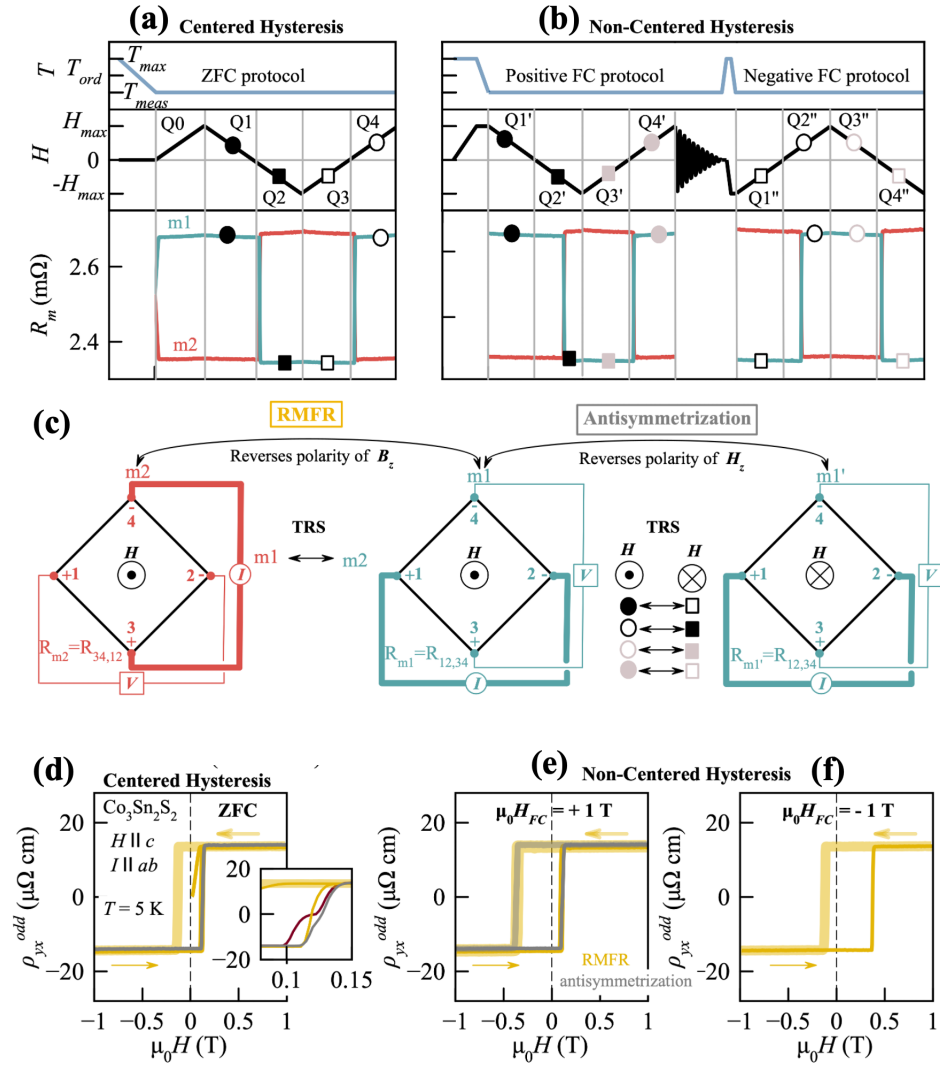


FIG. 3. Generic time (t) histories of magnetic field (H) and temperature (T) for (a, top axis) the zero-field-cooled (ZFC) protocol and (b, top axis) the positive and negative field-cooled (FC) protocols. For $\text{Co}_3\text{Sn}_2\text{S}_2$ with applied field $H \parallel c$, $\mu_0 H_{max} = 1 \text{ T}$, $T_{max} = 300 \text{ K}$, and $T_{meas} = 5 \text{ K}$, the ZFC protocol yields centered hysteresis loops whereas FC protocols yield non-centered loops. Q labels indicate the measurement order of the field-sweep segments: for ZFC, Q0 denotes $0 \rightarrow +1 \text{ T}$, followed by Q1–Q4: $+1 \text{ T} \rightarrow 0$, $0 \rightarrow -1 \text{ T}$, $-1 \text{ T} \rightarrow 0$, and $0 \rightarrow +1 \text{ T}$. For the positive FC protocol, Q1'–Q4' use the same segment definitions as Q1–Q4 but without Q0. For the negative FC protocol, Q1''–Q4'' sequentially label $-1 \text{ T} \rightarrow 0$, $0 \rightarrow +1 \text{ T}$, $+1 \text{ T} \rightarrow 0$, and $0 \rightarrow -1 \text{ T}$. Corresponding histories of the measured resistances R_m , labeled m1 (blue) and m2 (red), used to extract the Hall resistivity ρ_{yx}^{odd} of $\text{Co}_3\text{Sn}_2\text{S}_2$ are shown for (a, bottom axis) the ZFC protocol and (b, bottom axis) the positive and negative FC protocols. The measurements were performed with current $I \parallel ab$. Shown for a Van der Pauw geometry (c), m1 and m2 correspond to $R_{m1} = R_{12,34}$ and $R_{m2} = R_{34,12}$, where the first index pair denotes the current source and drain contacts and the second index pair denotes the high and low voltage contacts. (c) Schematic comparison of reverse-magnetic-field reciprocity (RMFR) and antisymmetrization methods for extracting the Hall effect. The RMFR method uses m1 and the I – V -rotated measurement m2 to generate a pair of measurements equivalent to reversing the polarity of B_z resulting in time-reversed states (TRS), while antisymmetrization uses m1 and m1' measured with the same contact geometry at equal and opposite H to measure TRS. Depending on whether the hysteresis loops are centered or non-centered, one or two hysteresis loops are required to access H -dependent TRS; the TRS pairing used in (a,b) is encoded according to the legend in (c). ρ_{yx}^{odd} obtained from R_m in (a,b) for (d) the ZFC protocol, (e) the positive FC protocol with $\mu_0 H_{FC} = +1 \text{ T}$, and (f) the negative FC protocol with $\mu_0 H_{FC} = -1 \text{ T}$. Yellow curves in (d–f) are obtained using RMFR, while gray curves are obtained using antisymmetrization. Thick lines denote sweeps from $+1 \text{ T} \rightarrow -1 \text{ T}$, and thin lines denote $-1 \text{ T} \rightarrow +1 \text{ T}$. The inset of (e) highlights the coercive-field region; the maroon data are an independent measurement using the antisymmetrization method.

shown schematically in Figure 3c for a VdP geometry. Again, antisymmetrization also holds for Hall bar or more

arbitrary geometries. Like the RMFR method, antisymmetrization also assumes ohmic devices and appropriate

averaging techniques are used to eliminate thermoelectric voltages, where for our measurements we opt for the low-frequency AC lock-in method.

Although $M(H_z) \neq -M(-H_z)$ for all H_z in hysteretic materials, the experimental variable H_z can still be used to antisymmetrize the measured signal, but special care must be taken so that the system is prepared such that the Onsager-Casimir relations hold for H_z . In general, there are two possible scenarios: (1) where magnetic hysteresis loops are centered about $H = 0$ (the ZFC case of $\text{Co}_3\text{Sn}_2\text{S}_2$ [Figure 2a]) which we will refer to as centered hysteresis loops and (2) where the magnetic hysteresis is not centered about $H = 0$ (the EB case of $\text{Co}_3\text{Sn}_2\text{S}_2$ (Figure 2b,c) which we will refer to as non-centered hysteresis loops.

With the two methods introduced, we demonstrate how to extract the Hall effect shown in Figure 3d, for the centered hysteresis loop, and Figure 3e,f for the EB state of $\text{Co}_3\text{Sn}_2\text{S}_2$ using the decision tree presented in Figure 4.

A. Case 1: centered hysteresis loops

Figure 4 presents a generic flow chart for the steps in measuring the Hall effect, where we first recommend measuring $M(H)$ (Box 1) for the same H orientation and history $H - T$ for which it is desired to measure the Hall effect. Since the Hall effect cannot be measured directly without perfectly aligned contacts, $M(H)$ is a convenient method of checking for hysteresis as it can be measured without any data manipulation and the Hall effect directly depends on it through B . If it is not possible to measure $M(H)$ on your sample, measuring $R_{xx}(H)$ in a collinear geometry where all contacts span the entire width of the sample to minimize the parasitic Hall voltages, is the next best thing to check for hysteresis (Path 1-2'). Either way, measuring R_{xx} even if $M(H)$ can also be measured (Path 1-2) is useful for converting the transport measurements to conductivity, but can also be used to diagnose artifacts as will be demonstrated later. If there is no hysteresis, $R_{yx}^{odd}(H)$ can be measured (1) with the RMFR method in a single field sweep from $0 \rightarrow H_{max}$ using Eq. 3 or (2) with antisymmetrization method sweeping from $-H_{max} \rightarrow H_{max}$ using Eq. 2. Either way, the $H - T$ path of the measurement should not matter since $M(+H) = M(-H)$ for all H . This is not the case in hysteretic materials, as will now be demonstrated.

Following Path 1-2-3-4 in Figure 4 we return to the ZFC loop of M and ρ_{xx} in Figure 2a, where the $H - T$ history of these measurements is plotted in Figure 3a. The measurements can be separated into five quadrants: $Q0$ ($0 \rightarrow H_{max}$), $Q1$ ($H_{max} \rightarrow 0$), $Q2$ ($0 \rightarrow -H_{max}$), $Q3$ ($-H_{max} \rightarrow 0$), and $Q4$ ($0 \rightarrow H_{max}$). Focusing on M in Figure 2a, it is apparent that $M(Q1) = -M(Q3)$ and $M(Q4) = -M(Q2)$, that is, these respective quadrants are TRS of each other. Note, that no TRS of $Q0$ is

present for such a ZFC hysteresis loop in M . Thus, to obtain R_{yx}^{odd} using antisymmetrization, R_{m1} , shown in Figure 3a, (blue), must be antisymmetrized in a piecewise manner using

$$R_{yx}^{odd}(H) = \begin{cases} \frac{R_{m1}(Q1, \bullet) - R_{m1}(Q3, \square)}{2} & \text{for } [Q1] \\ \frac{R_{m1}(Q2, \blacksquare) - R_{m1}(Q4, \circ)}{2} & \text{for } [Q2] \\ \frac{R_{m1}(Q3, \square) - R_{m1}(Q1, \bullet)}{2} & \text{for } [Q3] \\ \frac{R_{m1}(Q4, \circ) - R_{m1}(Q2, \blacksquare)}{2} & \text{for } [Q4]. \end{cases} \quad (4)$$

Analyzing Eq. 4, it is apparent that such a five quadrant hysteresis loop only produces two quadrants of *independent* data, either $R_{yx}^{odd}(Q1 \rightarrow Q2)$ or $R_{yx}^{odd}(Q3 \rightarrow Q4)$. By symmetry $R_{yx}^{odd}(Q1 \rightarrow Q2) = -R_{yx}^{odd}(Q3 \rightarrow Q4)$. While it is common practice to report all four quadrants, to emphasize the fact that only two quadrants of independent Hall data can be obtained by such a measurement of R_m , we only plot $\rho_{yx}^{odd}(Q3 \rightarrow Q4)$ in Figure 3d (gray) obtained by antisymmetrizing R_{m1} (Figure 3a, blue) using Eq. 4 and multiplying by the thickness of the sample.

By contrast, the RMFR method records R_{m1} (Figure 3a, blue) and R_{m2} (Figure 3a, red) simultaneously along the same ZFC $H - T$ history, allowing ρ_{yx}^{odd} , to be obtained via Eq. 3. The corresponding ρ_{yx}^{odd} is presented in Figure 3d (yellow). Notably, *independent* measurements of all five measurement quadrants are obtained. Mirroring M and ρ_{xx} (Figure 2a), ρ_{yx}^{odd} (Figure 3d) exhibits no exchange bias in the ZFC case of $\text{Co}_3\text{Sn}_2\text{S}_2$.

Overall, the RMFR method (yellow) and the antisymmetrization method (gray) agree within experimental accuracy on both the spontaneous ($H = 0$) AHE and the high-field value of ρ_{yx}^{odd} . However, differences emerge near the coercive fields (Figure 3d,inset): the RMFR yields a smooth sign reversal of ρ_{yx}^{odd} , whereas antisymmetrization shows a kink, and the coercive field obtained by the two methods is slightly offset. An independent Hall-bar measurement processed with the same antisymmetrization procedure (Eq. 4) accentuates these discrepancies (maroon curve in Figure 3d).

These deviations are naturally explained by a small trapped field in the superconducting magnet. Because antisymmetrization assumes perfectly opposite fields, the slight mismatch in switching fields where ρ_{xx} changes rapidly (Figure 2a) produces the observed kink. By construction, the RMFR pairs measurements that simulate an exactly reversed B_z at the same H_z (Figure 3c), mitigating this specific trapped-flux artifact. More broadly, anomalies around the coercive fields warrant caution as we will elaborate more on in the discussion. As for mitigating the coercive field issue, a finite offset in the magnitude of H_z is difficult to completely eliminate when using a superconducting magnet. It can be reduced by following the manufacturer's degaussing/ oscillation-to-zero procedures prior to measurement.

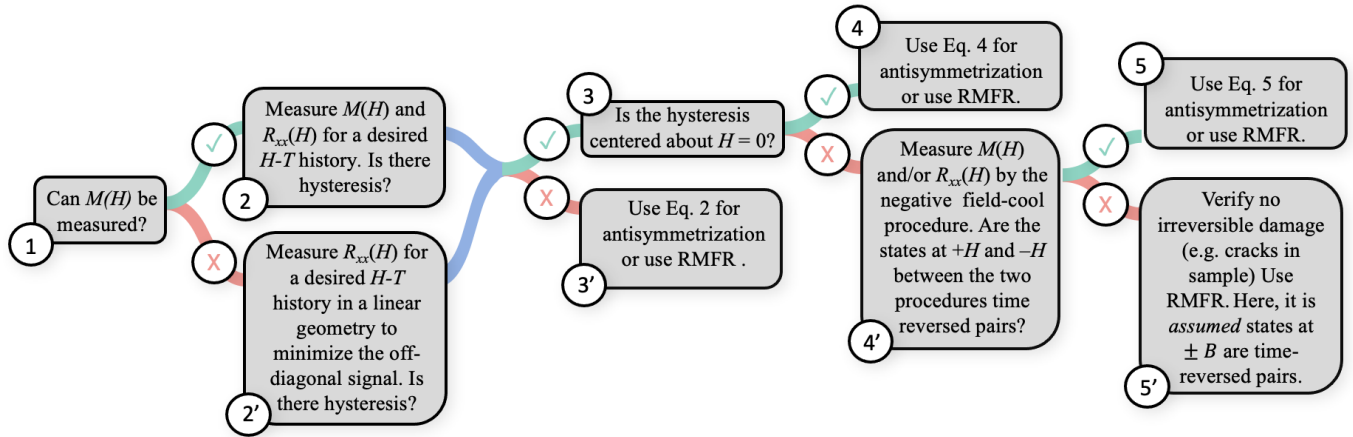


FIG. 4. A decision tree that can be used to minimize experimental artifacts in Hall effect measurements.

B. Case 2: Non-centered hysteresis loops

In the case where there is an EB effect or non-centered hysteresis loop in either M or ρ_{xx} (Path 1-2-3-4'-5 in Figure 4), as is the case for $\text{Co}_3\text{Sn}_2\text{S}_2$ in the field-cooled states (Figures 2b,c), two separate hysteresis loops are needed to extract the Hall effect if antisymmetrization is used: a positive field-cool protocol and negative field-cool protocol. For $\text{Co}_3\text{Sn}_2\text{S}_2$, the $H - T$ history for the positive and negative field-cool protocols is schematically shown in Figure 3b with $T_{max} = 300 \text{ K} > T_{ord} = T_c > T_{meas} = 5 \text{ K}$ and $\mu_0 H_{max} = \mu_0 H_{FC} = \pm 1 \text{ T}$. Explicitly, for the $\mu_0 H_{FC} = +1 \text{ T}$ case measurements are performed for $Q1'$ ($H_{max} \rightarrow 0$), $Q2'$ ($0 \rightarrow -H_{max}$), $Q3'$ ($-H_{max} \rightarrow 0$), and $Q4'$ ($0 \rightarrow H_{max}$), while for the $\mu_0 H_{FC} = -1 \text{ T}$ case we have $Q1''$ ($-H_{max} \rightarrow 0$), $Q2''$ ($0 \rightarrow H_{max}$), $Q3''$ ($H_{max} \rightarrow 0$), and $Q4''$ ($0 \rightarrow -H_{max}$). Here, we note that the ramp rate should always be kept constant between the positive and negative field cool procedures, as the dynamics in glassy systems can change with sweep rate. While most often non-centered hysteresis loops are found by field-cooling procedures, there are cases where EB has been reported in the ZFC state of systems [46, 47]. In such a case the positive field-cool protocols would include ZFCing the sample from above T_{ord} and running a hysteresis loop from $0 \rightarrow H_{max} \rightarrow -H_{max} \rightarrow H_{max}$ while the negative field-cool protocol would entail the loop from $0 \rightarrow -H_{max} \rightarrow H_{max} \rightarrow -H_{max}$.

Returning to the EB states in M for $\text{Co}_3\text{Sn}_2\text{S}_2$ (Figure 2b,c), it is apparent $M(Q1') \neq -M(Q3')$ and $M(Q2') \neq -M(Q4')$ for all H . Therefore, the states are not TRS and Eq 4 *cannot* be used. However, the TRS are prepared using the negative field-cooling protocol where it is demonstrated in Figure 2b,c $M(Q1') = -M(Q1'')$, $M(Q2') = -M(Q2'')$, $M(Q3') = -M(Q3'')$, $M(Q4') = -M(Q4'')$. Therefore, Onsager-Casimir reciprocity holds between such time-reversed states, and R_{yx}^{odd} can be extracted from R_{m1} :

$$R_{yx}^{odd}(H) = \begin{cases} \frac{R_m(Q1', \bullet) - R_m(Q1'', \square)}{2} & \text{for } H[Q1', \bullet] \\ \frac{R_m(Q2', \blacksquare) - R_m(Q2'', \circ)}{2} & \text{for } H[Q2', \blacksquare] \\ \frac{R_m(Q3', \blacksquare) - R_m(Q3'', \circ)}{2} & \text{for } H[Q3', \blacksquare] \\ \frac{R_m(Q4', \square) - R_m(Q4'', \bullet)}{2} & \text{for } H[Q4', \square] \\ \frac{R_{m1}(Q1'', \square) - R_m(Q1', \bullet)}{2} & \text{for } H[Q1'', \square] \\ \frac{R_{m1}(Q2'', \circ) - R_m(Q2', \blacksquare)}{2} & \text{for } H[Q2'', \circ] \\ \frac{R_{m1}(Q3'', \circ) - R_m(Q3', \blacksquare)}{2} & \text{for } H[Q3'', \blacksquare] \\ \frac{R_{m1}(Q4'', \bullet) - R_m(Q4', \square)}{2} & \text{for } H[Q4'', \bullet] \end{cases} \quad (5)$$

Again we emphasize that even though eight quadrants were measured, only four quadrants of *independent* data are obtained: either $Q1' \rightarrow Q4'$ or $Q1'' \rightarrow Q4''$. Hence, we plot ρ_{yx}^{odd} in Figure 3e (gray) only for $Q1' \rightarrow Q4'$ extracted from R_{m1} in Figure 3b using antisymmetrization by Eq. 5.

Using the RMFR method by measuring $m1$ (blue) and $m2$ (red) simultaneously for the same field-cool protocols in Figure 3b, two independent hysteresis loops for ρ_{yx}^{odd} are extracted using Eq. 3: one for $\mu_0 H_{FC} = +1 \text{ T}$ case (Figure 3e, yellow) and one $\mu_0 H_{FC} = -1 \text{ T}$ case (Figure 3f). In other words, the RMFR extracts double the *independent* data in the same time, or the same amount of *independent* data in half the time. Comparing the data to that obtained via the antisymmetrization method in gray, again the only differences appear near the coercive fields, with origins the same as the ZFC case.

The last scenario to discuss in Figure 4 is Path 1-2-3-4-5'. Such a situation could be encountered in an exceptionally hard ferromagnet with an ordering temperature above that which can be achieved in the cryostat being used. In this hypothetical situation, the magnet used for applying the field would not have a large enough field to reach the coercive field to flip the ferromagnetic domains, and it would be impossible to heat high enough to thermally disorder the ferromagnet. Therefore, the TRS

necessary for using the antisymmetrization method could never be accessed. Here, so long as there are no processes that irreversibly damage the sample (like cracks caused by strain), the RMFR method can still be used to measure the Hall effect.

With the two methods of extracting ρ_{yx}^{odd} demonstrated on $\text{Co}_3\text{Sn}_2\text{S}_2$, we next use CeCoGe_3 as an example of how improper antisymmetrization can lead to artifacts that mimic the AHE.

IV. CeCoGe_3

CeCoGe_3 crystallizes in the tetragonal, non-centrosymmetric BaNiSn_3 -type structure (space group $I4mm$) [28], consistent with our X-ray diffraction experiments (Figure S2, Tables S5-8). In this structure, the Ce atoms occupy the four corners and the body center of the tetragonal unit cell. The Co-Ge connectivity is asymmetric around the body-centered Ce along the crystallographic c -axis, breaking inversion symmetry [28]. This lack of centrosymmetry introduces the Dzyaloshinskii-Moriya (DM) interaction [48, 49], which competes with the Heisenberg-like RKKY interaction. Such competition can, in turn, lead to exotic domains or magnetic textures such as non-coplanar spin textures including skyrmions with application of a magnetic field [50-53].

Indeed, the $H - T$ phase diagram of CeCoGe_3 with $H \parallel c$ has been found to be complex [29]. For $H = 0$, RKKY interactions induce long-range magnetic order below $T_N = 21$ K with a temperature-dependent evolution of magnetic structures [28, 29, 54]. The ground state, which exists below 8 K, is characterized by a magnetic propagation vector \mathbf{k} (0,0,1/2) with a proposed two-up two-down magnetic structure [54]. With application of a magnetic field $H \parallel c$, three metamagnetic transitions have been reported below 8 K [29]. With competing energy scales and a complex $H - T$ phase diagram, CeCoGe_3 is a natural platform to search for non-coplanar spin textures, for which the Hall effect is a convenient first probe in most labs. Before presenting the Hall measurements, we first demonstrate that due to non-centered hysteresis caused by certain field-cooling procedures in M and ρ_{xx} about $H = 0$, measuring the Hall effect in CeCoGe_3 is not straightforward.

Figures 5a,b show isothermal M and ρ_{xx} , respectively, measured for $H \parallel c$ using the positive field cool procedure (Figure 3b) with $T_{max} = 100$ K, $T_{meas} = 3$ K, and $\mu_0 H_{max} = \mu_0 H_{FC} = 4$ T, where $\mu_0 H_{FC}$ is above the highest metamagnetic transition. The low H metamagnetic transitions for $Q4'$ [Figure 5a,b (main panel, dark lines)] are registered as anomalies in both M and ρ_{xx} near $\mu_0 H_{c1} \sim 0.16$ T and $\mu_0 H_{c2} \sim 0.8$ T, while the higher H metamagnetic transition near $\mu_0 H_{c3} \sim 3$ T is highlighted in the insets of Figures 5a,b, consistent with previous measurements [29]. It is clear that the magnitude of $\mu_0 H_{c1}$ and $\mu_0 H_{c2}$ change between measurements taken

$Q4'$ (dark lines) compared to the data taken with $Q1'$ (light lines) consistent with a first-order phase transition. More striking is the fact that $M(Q1') \neq -M(Q3')$ and $M(Q2') \neq -M(Q4')$ near $\mu_0 H = 0$ T [Figure 5a (main panel)]. Similarly, as seen in [Figure 5b (main panel)], a zero-field hysteresis is observed and $\rho_{xx}(Q1') \neq \rho_{xx}(Q3')$, $\rho_{xx}(Q2') \neq \rho_{xx}(Q4')$. The origins of this unusual asymmetry are due to glassy-like magnetic phase coexistence from a first-order phase transition and the details will be reported elsewhere.

Nonetheless, while TRS cannot be achieved in a single hysteresis loop, similar to the field-cooled cases of $\text{Co}_3\text{Sn}_2\text{S}_2$, following Path 1-2-3-4' in Figure 4, the TRS can be found. Figures 5c,d show M and ρ_{xx} , respectively, for the $\mu_0 H_{FC} = -4$ T (negative) field cool procedure. Comparing M in Figure 5a and 5c, it is apparent $M(Q1') = -M(Q1'')$, $M(Q2') = -M(Q2'')$, $M(Q3') = -M(Q3'')$, and $M(Q4') = -M(Q4'')$. Likewise $\rho_{xx}(Q1') = \rho_{xx}(Q1'')$, $\rho_{xx}(Q2') = \rho_{xx}(Q2'')$, $\rho_{xx}(Q3') = \rho_{xx}(Q3'')$, and $\rho_{xx}(Q4') = \rho_{xx}(Q4'')$, as can be seen in comparing Figures 5b,d, confirming these respective states are indeed TRS of each other. Therefore, if it is desired to extract ρ_{yx}^{odd} , using antisymmetrization, Eq. 5 (Path 1-2-3-4'-5 in Figure 4) should be applied to the raw data after taking the two measurements with the $\mu_0 H_{FC} = +4$ T and $\mu_0 H_{FC} = -4$ T field-cooling procedures.

The corresponding Hall resistivity ρ_{yx}^{odd} is presented in Figure 6a where the raw data was collected in a Hall bar geometry using the low-frequency AC lock-in detection method and processed using the antisymmetrization method with Eq. 5. ρ_{yx}^{odd} displays a non-linear dependence on H , consistent with a multi-carrier response, shows little sensitivity to the metamagnetic transitions at $\mu_0 H_{c1}$ and $\mu_0 H_{c2}$, and exhibits a more pronounced change at $\mu_0 H_{c3}$. Notably, $\rho_{yx}^{odd}(0) = 0$ (no AHE) even though $\rho_{xx}(0)$ and $M(0)$ show zero-field hysteresis. We confirmed that there is no AHE in an independent crystal using RMFR with a VdP geometry shown in Figure S3 of the Supplementary Materials. While the mobilities, and hence, the curvature of ρ_{yx}^{odd} may vary from crystal to crystal, the lack of the AHE and qualitative behavior ρ_{yx}^{odd} are consistent.

This scenario of no AHE even though $\rho_{xx}(0)$ and $M(0)$ exhibit hysteresis is plausible if whatever mechanism is responsible for the AHE, whether intrinsic or extrinsic averages to zero due to domain averaging in real-space, or is symmetry forbidden. We leave the exact mechanism to future studies, but move on to demonstrate, that incorrect treatment of the data can lead to a false AHE.

If it was not realized that CeCoGe_3 exhibits non-centered hysteresis loops by measuring M and ρ_{xx} with the same field-cooling procedure, one may be tempted to use Eq. 4 which is only valid for centered hysteresis loops, to antisymmetrize the R_m data. Doing so results in the traces shown in Figures 6c,d for $\mu_0 H_{FC} = +4$ T and $\mu_0 H_{FC} = -4$ T, respectively, where we have labeled the curves as ΔR_m to emphasize that ΔR_m does

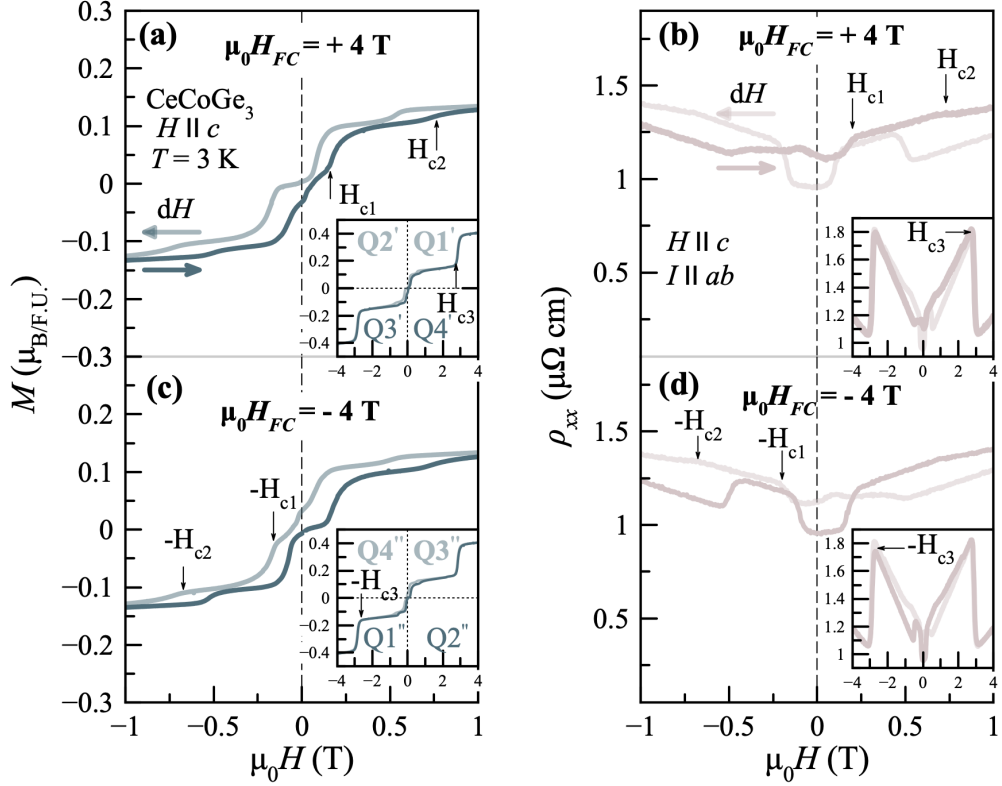


FIG. 5. (a) Isothermal magnetization (M) and (b) longitudinal resistivity (ρ_{xx}) measured at temperature $T = 3$ K after cooling the sample from 100 K in $\mu_0 H_{FC} = +4$ T using the positive field cool procedure. $Q1' - Q4'$ in (a) label the sequential quarter-segments of the field sweep; $+4$ T \rightarrow 0, 0 \rightarrow -4 T, -4 T \rightarrow 0, and 0 \rightarrow $+4$ T, respectively. (c) M and (d) ρ_{xx} after field-cooling the sample in $\mu_0 H_{FC} = -4$ T using the negative field cool procedure. $Q1'' - Q4''$ in (c) label the sequential quarter-segments of the field sweep; -4 T \rightarrow 0, 0 \rightarrow 4 T, 4 T \rightarrow 0, and 0 \rightarrow -4 T (c) for the negative field-cool protocol. The main panels show data from $\mu_0 H = \pm 1$ T, while the insets show the same data from $\mu_0 H = \pm 4$ T. Light lines in all panels correspond to data measured from $+4$ T \rightarrow -4 T while dark lines correspond to -4 T \rightarrow $+4$ T. All measurements were performed with the applied magnetic field $H \parallel c$ while the transport measurements were performed with the current $I \parallel ab$. Anomalies corresponding to metamagnetic transitions for increasing H and $H > 0$ or decreasing H and $H < 0$ are labeled as H_{c1} , H_{c2} , H_{c3} and $-H_{c1}$, $-H_{c2}$, $-H_{c3}$, respectively.

not correspond to the true Hall effect ρ_{yx}^{odd} in this case. If ΔR_m were incorrectly interpreted as ρ_{yx}^{odd} , a clear AHE would be deduced in the zero-field limit, and it could be tempting to possibly attribute other $H > 0$ features to the THE. Given the hysteresis in M and the non-centrosymmetric crystal structure, such a scenario could be possible. However, as already demonstrated in Figure 6a, correctly processing R_m eliminates the possibility of an AHE or THE in CeCoGe₃. The artifact clearly originates from the hysteresis in ρ_{xx} . This comparison demonstrates the importance of correctly processing raw Hall data to eliminate artifacts and incorrect conclusions, and emphasizes the importance of measuring and reporting other thermodynamic or transport properties measured under the same $H - T$ history.

V. DISCUSSION

A. Artifacts-how to spot them and how to correct them

As demonstrated, a central difficulty in extracting the Hall effect in hysteretic materials is that measurements taken at opposite fields, $+H$ and $-H$, are not guaranteed to represent time-reversed states. In hysteretic materials $M(H) \neq -M(-H)$ for all H . In such cases a naive antisymmetrization at $\pm H$ in a single field sweep can lead to artifacts like that shown in Figure 1a. Here, we have emphasized the idea of TRS, so that Onsager-Casimir reciprocal relations which are strictly valid for states at $\pm B$ can be applied for the controlled variable H . RMFR enforces time reversal by swapping current and voltage contacts between two otherwise identical measurements, which is equivalent to reversing the polarity of B_z at the same applied field (H_z) setpoint. Therefore, RMFR

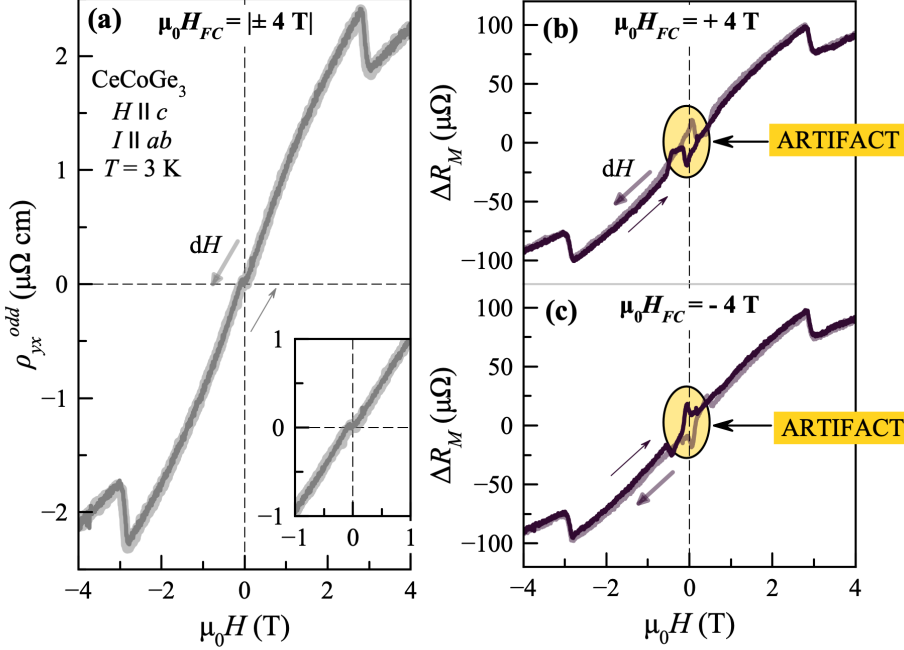


FIG. 6. (a) Isothermal Hall resistivity ρ_{yx}^{odd} of CeCoGe₃ extracted using antisymmetrization with Eq. 5 measured at temperature $T = 3$ K with magnetic field $H \parallel c$ and current $I \parallel ab$ after field cooling the sample in $\mu_0 H_{FC} = |\pm 4|$ T. The inset is the same data zoomed in around zero-field showing there is no anomalous Hall effect. ΔR_m obtained by improper use of Eq. 4 under (b) the positive field-cool protocol with $\mu_0 H_{FC} = +4$ T and (c) the negative field-cool protocol with $\mu_0 H_{FC} = -4$ T. Artifacts generated from improper antisymmetrization in (b-c) are highlighted in yellow. Light lines in all panels correspond to data measured from $+4$ T \rightarrow -4 T while dark lines correspond to -4 T \rightarrow $+4$ T.

provides a robust method of extracting the Hall effect in a single hysteresis loop whether or not the hysteresis is centered about $H = 0$. The only requirements for using the RMFR method are that the sample and contacts are Ohmic and that the resistivity tensor obeys Onsager-Casimir reciprocity [27]. For violations of these conditions we refer you to a recent review on non-linear transport [55]. Antisymmetrization, which has the same requirements, remains useful since it can be done with only one measurement channel, but care must be taken to assure the data is antisymmetrized between only TRS. We have provided a decision tree and field cooling protocols to explain how TRS states can be achieved in Figure 3.

The comparison of the two methods on Co₃Sn₂S₂ clarifies the trade-offs between the two methods. In the ZFC case where the hysteresis loops are centered, we have followed Path 1-2-3-4 in Figure 4. Piecewise antisymmetrization reproduces the RMFR result away from coercivity, confirming ρ_{yx}^{odd} is captured correctly when time-reversal pairing is respected (Figure 2e). Once EB is introduced by field cooling (Path 1-2-3-4'-5 in Figure 4), the loop is no longer centered about $H = 0$ (Figure 3e,f). RMFR continues to isolate ρ_{yx}^{odd} reliably in a single hysteresis loop, while antisymmetrization requires over double the time since two hysteresis loops of R_m need to be

measured in reverse field-cool procedures with respect to each other where the sample would have to be warmed above the ordering temperature and the field oscillated to zero between. These facts highlight two advantages of the RMFR method - ρ_{yx}^{odd} can be captured over twice as fast and no a priori knowledge of whether the hysteresis loops are centered or not is needed.

The two methods diverge, most notably as kinks near the coercive fields. Here, one typically finds a mundane cause: residual field in the superconducting magnet subtly coupled with a sharp feature in magnetoresistance, imprinting features that antisymmetrization cannot cancel (Figure 3d, inset). The RMFR method inherently mitigates the problem because it measures an R equivalent to exactly an opposite B at the same nominal H . More broadly, anomalies around the coercive fields warrant caution: features such as bumps are often attributed to a topological Hall contribution [56–59], while alternative explanations for some cases have been proposed [60, 61]. Regardless of the underlying physics, minimizing instrumental artifacts is essential for interpretation.

While we focused on magnetic materials in this work, it should be noted that trapped flux together with a large magnetoresistance, can cause artifacts in Hall measurements when using antisymmetrization methods even in

non-magnetic materials. If enigmatic Hall data is measured in such a scenario, it is worth checking a measurement using RMFR to make sure the data is correct.

The CeCoGe₃ case illustrates the broader lesson for materials with glassy or coexisting magnetic domains with strong pinning. Such a scenario may happen when there is magnetic frustration, disorder, magnetic phase coexistence, or near first-order phase transitions. Here, we demonstrated the importance of reporting $M(H)$ and the longitudinal resistivity $\rho_{xx}(H)$ (Figure 5) together with ρ_{yx}^{odd} (Figure 6a). In measuring $\rho_{xx}(H)$ and $M(H)$ we were able to deduce the apparent AHE-like signature registered in ΔR_m (Figure 6b,c) arises from asymmetric $\rho_{xx}(H)$.

B. Contact geometry

The methods presented here only work for extracting the Hall effect, ρ_{yx}^{odd} . In materials with low enough symmetry as described in Section I, ρ_{yx} can have even-in- B_z anisotropic magnetoresistive terms which are necessarily canceled by both the RMFR and antisymmetrization techniques. Careful consideration of the contact geometry would be needed to extract the full resistivity tensor.

When only the Hall effect, ρ_{yx}^{odd} , is desired, the Onsager-Casimir reciprocal relation [13, 15–17] $\rho_{yx}^{odd}(B_z) = -\rho_{xy}^{odd}(B_z)$, implies ρ_{yx}^{odd} is independent of current direction, and therefore can be extracted with arbitrary contact placement, as long as B_z is parallel to the face-normal of the xy -plane, and the voltage contacts are placed in such a way to pick up some transverse signal.

The choice of whether to choose between, for example, a VdP geometry or Hall bar geometry depends on how large the transverse voltage is relative to the longitudinal voltage. For reference of what these geometries can look like in practice, images of the contact geometries used for measurements on Co₃Sn₂S₂ are shown in Figure S4. If the transverse voltage is large, either geometry is equally valid, but a VdP geometry has the advantage of being able to measure the anisotropic resistivity via the Montgomery method [62, 63] and the Hall effect with the same contacts. On the other hand, if the transverse voltage is small compared to the longitudinal voltage, a Hall bar geometry can be used to minimize the relative size of the longitudinal signal in the measured signal. This comes at the cost of having to put more contacts on to measure any resistivity anisotropies.

Also, ρ_{yx}^{odd} can be obtained by multiplying R_{yx}^{odd} by the thickness of the crystal in either VdP or Hall bar geometry. The assumptions are that the sample is uniform and ohmic with well-defined thickness.

C. Anomalous and Topological Hall effects

We only covered how to reliably measure the total Hall effect ρ_{yx}^{odd} . Historically, $\rho_{yx}^{odd} = \rho_{yx}^N + \rho_{yx}^{AHE} + \Delta\rho_{yx}$, has been divided into three contributions. The first term ρ_{yx}^N is the normal Hall effect [64] which arises due to the Lorentz force electrons experience in a magnetic field. ρ_{yx}^{AHE} arises from reciprocal-space Berry curvature, skew scattering or side-jump scattering, and typically depends on M . $\Delta\rho_{yx}$ are terms that do not depend on M . For detailed discussions, analysis and interpretation of ρ_{yx}^{AHE} , we refer to Ref. [8, 9]. $\Delta\rho_{yx}$ can either come from the real-space topology of magnetic structures, sometimes called the THE or more generally from net SSC in non-coplanar spin textures, for which real-space topological spin textures are a special case. Here, we refer to Refs. [11, 65–67]. Finally, Hall effects can emerge in antiferromagnets with exceedingly small magnetization that are not related to ρ_{yx}^N , and therefore, by the previous definition, would fall into the $\Delta\rho_{yx}$ category. However, this phenomenon is referred to as the AHE since its origins are reciprocal-space Berry curvature as reviewed in [2]. The physics and history of measuring the Hall effect is vast and quickly evolving. We therefore do not attempt a complete list of relevant references. However, it is worth cautioning not to overinterpret $\Delta\rho_{yx}$ since there can be many origins [60, 68–70].

D. Relevance to transition-metal intercalated transition metal dichalcogenides

The Hall analysis procedures described here are generic and applicable to any conductor, but they are indispensable in hysteretic materials. As noted in the Introduction, EB was first associated with engineered AFM/FM thin-film heterostructures [20], but it has recently been shown in single-crystalline magnetic conductors as well [21–26]. A particularly promising platform for exploring EB, or more generally, non-centered hysteresis and related functionalities is the family of transition-metal–intercalated transition metal dichalcogenides (TMDs). Parkin and Friend showed in 1980 that magnetic intercalation in TMDs produces highly anisotropic layered magnets with large AHE responses [71–73]. Subsequent work has revealed a rich variety of spin textures and domain states controlled by host material and intercalant concentration. Representative examples include AHE or THE signals from non-coplanar spin textures in Cr_{1/3}NbS₂, Co_{1/3}TaS₂, and Cr_{1/3}TaS₂ [74–80], as well as sharp magnetic switching accompanied by an AHE in the hard ferromagnet Fe_{1/4}TaS₂ [81–84]. These materials therefore provide a natural arena where Hall measurements directly probe magnetic order and domain physics.

At the same time, their sensitivity to stoichiometry and disorder makes the phase space highly tunable, but prone to non-centered hysteresis. Phase coexistence and disor-

der are precisely the ingredients that can generate non-centered hysteresis loops, especially if measurements are done in the field-cooled state. For example, $\text{Fe}_{1/3+\delta}\text{NbS}_2$ develops a coupled spin-glass/antiferromagnetic state that yields giant EB and enables energy-efficient electrical switching [23, 85], with magnetic domains acutely sensitive to stoichiometry [86]. $\text{V}_{1/3}\text{NbS}_2$ hosts a multido- main state producing a spontaneous AHE emerging from a non-Fermi-liquid regime [87], while $\text{Cr}_{1/4}\text{TaS}_2$ shows AHE and glassy behavior associated with magnetic phase coexistence [88]. Room-temperature exchange bias has also been reported in $\text{Fe}_{0.17}\text{ZrSe}_2$ [89]. Given that intercalated TMDs already exhibit both exotic spin textures and EB, similar physics is likely across other compositions. The methods presented enable measurement of the Hall effect in the EB state, and will be exceptionally useful to distinguish intrinsic effects from measurement artifacts in this material family as well as others with similar interplay of complex magnetism, stoichiometry, and disorder.

VI. CONCLUSIONS

We have shown that extracting the true odd-in-field Hall response in hysteretic magnetic materials is not as simple as antisymmetrizing $R_m(+H)$ with $R_m(-H)$ because opposite applied fields do not necessarily prepare time-reversed magnetic states once there is coercivity, exchange bias, glassiness, or multi-step metamagnetism. As a result, incorrect processing can generate AHE or THE-like artifacts that result from uncompensated longitudinal signals in the measured voltages. We addressed this by laying out two practical routes - (1) the RMFR method and (2) antisymmetrization of time-reversed states in an applied magnetic field. We provide a workflow to record intrinsic Hall voltages from measurements. These methods are general and will be useful in characterizing magnetic conductors.

VII. METHODS

A. Crystal Growth

$\text{Co}_3\text{Sn}_2\text{S}_2$ was grown out of a ternary melt [90]. The constituent elements were weighed in the ratio $\text{Co}_{12}\text{Sn}_{80}\text{S}_6$, put in an alumina crucible, and sealed in an evacuated quartz tube. The ampoule was heated to 400°C over 2 hrs and held for 2 hrs, then ramped to 1050°C over 6 hrs and dwelled for 10 hrs. It was subsequently cooled to 700°C over 60 hrs, at which point the remaining flux was separated by centrifugation.

CeCoGe_3 was grown from Bi flux [29, 91]. Ce:Co:Ge were weighed in the stoichiometric molecular ratio of 1:1:3 and arc melted in an Ar atmosphere. The mass loss after arc melting was 2.8%. The arc melted bead was

then put in an alumina crucible with Bi such that the total loaded composition was $\text{Ce}_6\text{Co}_6\text{Ge}_{18}\text{Bi}_{70}$. The growth was sealed in an evacuated quartz ampoule, heated to 1150°C at 120°C/hr where it dwelled for 5 hrs, before cooling to 650°C over 148 hrs where it was centrifuged to separate the crystals from the flux.

B. X-ray diffraction

Single crystal X-ray diffraction measurements were performed at room temperature or 100 K using a Rigaku XtaLAB Synergy-S/i diffractometer equipped with a Mo $\text{K}_{\alpha 1}$ ($\lambda = 0.71073 \text{ \AA}$), micro-focus sealed-tube X-ray source and a graphite monochromator. Integration was carried out using CrysAlis^{Pro} software, with numerical absorption correction based on Gaussian integration over a multifaceted crystal model. Full structural refinements on F^2 were performed in JANA2020.

C. Electrical Transport

A single crystal of $\text{Co}_3\text{Sn}_2\text{S}_2$ was shaped into an approximate rectangular plate. For the Hall measurements on $\text{Co}_3\text{Sn}_2\text{S}_2$ electrical contacts were attached in the ab -plane in a VdP geometry using silver paint and gold wires. Measurements were done in a Quantum Design (QD) DynaCool physical properties measurement system (PPMS) cryostat using a Lake Shore M81-SSM synchronous source measure system equipped with BCS-10 balanced current source modules and VM-10 voltage measure modules. The two current sources were set with 10 mA amplitudes running at different frequencies (17.17 Hz and 7.717 Hz). The two voltage measurement modules were locked into the respective frequencies while setting the ground to the voltage sink in m1 (V-), or equivalently, the current sink in m2 (I-) (Figure 3c) using the Common-Mode Rejection feature of the M81-SSM allowing for simultaneous acquisition of m1 and m2. The magnetic field was swept at 50 Oe/s. The independent Hall bar measurement in Figure 3d was measured on the same crystal. The methods for extracting the Hall resistivity are discussed in the paper. Because the Hall voltage is so large in $\text{Co}_3\text{Sn}_2\text{S}_2$, a collinear geometry was used for measurements of the longitudinal resistivity. Even still, the raw signal must be symmetrized using

$$R_{xx}(H) = \begin{cases} \frac{+(+)R_m(Q1) + (+)R_m(Q3)}{2} & \text{for } H[Q1, (Q3)] \\ \frac{+(+)R_m(Q2) + (+)R_m(Q4)}{2} & \text{for } H[Q2, (Q4)], \end{cases} \quad (6)$$

for the ZFC case, and

$$R_{xx}(H) = \begin{cases} \frac{(+R_m(Q1') + (+R_m(Q1''))}{2} & \text{for } H[Q1', (Q1'')] \\ \frac{(+R_m(Q2') + (+R_m(Q2''))}{2} & \text{for } H[Q2', (Q2'')] \\ \frac{(+R_m(Q3') + (+R_m(Q3''))}{2} & \text{for } H[Q3', (Q3'')] \\ \frac{(+R_m(Q4') + (+R_m(Q4''))}{2} & \text{for } H[Q4', (Q4'')], \end{cases} \quad (7)$$

for the EB cases.

Since the Hall voltage is small compared to the longitudinal voltage in CeCoGe_3 we opted for a Hall bar geometry where electrical contacts were attached in the ab -plane using gold paint and the signals were acquired using the low-frequency lock-in detection method ($f = 15.259$ Hz with a $I = 5$ mA current) in a QD DynaCool PPMS using the ETO option. The magnetic field was swept at 25 Oe/s. Hall data was antisymmetrized using the methods described in the text. Magnetoresistance was measured with the same parameters in a collinear geometry and was not symmetrized.

D. Magnetization

Magnetization measurements were performed in a QD magnetic measurement system (MPMS) equipped with the VSM-SQUID option. Samples were mounted on either a brass holder for $\text{Co}_3\text{Sn}_2\text{S}_2$, or a quartz holder for CeCoGe_3 using GE varnish. The magnetic field was

swept at 50 Oe/s or 25 Oe/s respectively.

VIII. ACKNOWLEDGMENTS

This work was supported by the Air Force Office of Scientific Research under award number A9550-23-1-0635. Additional support was provided by an NSF CAREER grant (DMR-2144295) to LMS and the Gordon and Betty Moore Foundation's EPIQS initiative through Grant GBMF9064. We thank Jeffrey Lindemuth and Emilio A. Codecido for useful discussions.

IX. FINANCIAL DISCLOSURE

None reported.

X. CONFLICT OF INTEREST

The authors declare no potential conflict of interests.

XI. DATA AVAILABILITY

All thermodynamic and transport data used in this manuscript will be made available publicly upon publication.

-
- [1] Jeon JC, Migliorini A, Yoon J, Jeong J, Parkin SS. Multicore memristor from electrically readable nanoscopic racetracks. *Science*. 2024;386(6719):315–322.
- [2] Šmejkal L, MacDonald AH, Sinova J, Nakatsuji S, Jungwirth T. Anomalous hall antiferromagnets. *Nature Reviews Materials*. 2022;7(6):482–496.
- [3] Šmejkal L, Mokrousov Y, Yan B, MacDonald AH. Topological antiferromagnetic spintronics. *Nature physics*. 2018;14(3):242–251.
- [4] Liu CX, Zhang SC, Qi XL. The quantum anomalous Hall effect: theory and experiment. *Annual Review of Condensed Matter Physics*. 2016;7(1):301–321.
- [5] Karsenty A. A comprehensive review of integrated Hall effects in macro-, micro-, nanoscales, and quantum devices. *Sensors*. 2020;20(15):4163.
- [6] Chang CZ, Zhang J, Feng X, et al. Experimental observation of the quantum anomalous Hall effect in a magnetic topological insulator. *Science*. 2013;340(6129):167–170.
- [7] Deng Y, Yu Y, Shi MZ, et al. Quantum anomalous Hall effect in intrinsic magnetic topological insulator MnBi_2Te_4 . *Science*. 2020;367(6480):895–900.
- [8] Nagaosa N, Sinova J, Onoda S, MacDonald AH, Ong NP. Anomalous hall effect. *Reviews of modern physics*. 2010;82(2):1539–1592.
- [9] Xiao D, Chang MC, Niu Q. Berry phase effects on electronic properties. *Reviews of modern physics*. 2010;82(3):1959–2007.
- [10] Neubauer A, Pfeiderer C, Binz B, et al. Topological Hall effect in the A phase of MnSi . *Physical review letters*. 2009;102(18):186602.
- [11] Taguchi Y, Oohara Y, Yoshizawa H, Nagaosa N, Tokura Y. Spin chirality, Berry phase, and anomalous Hall effect in a frustrated ferromagnet. *Science*. 2001;291(5513):2573–2576.
- [12] Kao LP, Katz E. Phenomenological theory of anisotropic isothermal galvanomagnetic effects. *Journal of Physics and Chemistry of Solids*. 1958;6(2-3):223–235.
- [13] Akgoz Y, Saunders G. Space-time symmetry restrictions on the form of transport tensors. I. Galvanomagnetic effects. *Journal of Physics C: Solid State Physics*. 1975;8(9):1387.
- [14] Gallego SV, Etxebarria J, Elcoro L, Tasçi ES, Pérez-Mato JM. Automatic calculation of symmetry-adapted tensors in magnetic and non-magnetic materials: a new tool of the Bilbao Crystallographic Server. *Foundations of Crystallography*. 2019;75(3):438–447.
- [15] Onsager L. Reciprocal relations in irreversible processes. I.. *Physical review*. 1931;37(4):405.
- [16] Onsager L. Reciprocal relations in irreversible processes. II.. *Physical review*. 1931;38(12):2265.
- [17] Casimir HBG. On Onsager's principle of microscopic reversibility. *Reviews of Modern Physics*. 1945;17(2-3):343.

- [18] Czajka P, Gao T, Hirschberger M, et al. Oscillations of the thermal conductivity in the spin-liquid state of α -RuCl₃. *Nature Physics*. 2021;17(8):915–919.
- [19] Singha R, Dalgaard KJ, Marchenko D, et al. Colossal magnetoresistance in the multiple wave vector charge density wave regime of an antiferromagnetic Dirac semimetal. *Science Advances*. 2023;9(41):eadh0145.
- [20] Nogués J, Schuller IK. Exchange bias. *Journal of Magnetism and Magnetic Materials*. 1999;192(2):203–232.
- [21] Lachman E, Murphy RA, Maksimovic N, et al. Exchange biased anomalous Hall effect driven by frustration in a magnetic kagome lattice. *Nature communications*. 2020;11(1):560.
- [22] Noah A, Toric F, Feld TD, et al. Tunable exchange bias in the magnetic Weyl semimetal Co₃Sn₂S₂. *Physical Review B*. 2022;105(14):144423.
- [23] Maniv E, Murphy RA, Haley SC, et al. Exchange bias due to coupling between coexisting antiferromagnetic and spin-glass orders. *Nature Physics*. 2021;17(4):525–530.
- [24] Xu X, Yang S, Wang H, et al. Ferromagnetic-antiferromagnetic coexisting ground state and exchange bias effects in MnBi₄Te₇ and MnBi₆Te₁₀. *Nature Communications*. 2022;13(1):7646.
- [25] Firdosh N, Sinha S, Sinha I, Singh M, Patnaik S, Manna S. Exchange bias and anomalous Hall effect driven by intertwined magnetic phases in MnBi₄Te₇. *Physical Review B*. 2025;112(14):144410.
- [26] Kotegawa H, Kuwata Y, Huyen VTN, et al. Large anomalous Hall effect and unusual domain switching in an orthorhombic antiferromagnetic material NbMnP. *npj Quantum Materials*. 2023;8(1):56.
- [27] Sample H, Bruno W, Sample S, Sichel E. Reverse-field reciprocity for conducting specimens in magnetic fields. *Journal of applied physics*. 1987;61(3):1079–1084.
- [28] Pecharsky V, Hyun OB, Gschneidner Jr K. Unusual magnetic properties of the heavy-fermion compound CeCoGe₃. *Physical Review B*. 1993;47(18):11839.
- [29] Thamizhavel A, Takeuchi T, D Matsuda T, et al. Unique magnetic phases in an antiferromagnet CeCoGe₃. *Journal of the Physical Society of Japan*. 2005;74(6):1858–1864.
- [30] Weihrich R, Anusca I. Half antiperovskites. III. Crystallographic and electronic structure effects in Sn_{2-x}In_xCo₃S₂. *Zeitschrift für anorganische und allgemeine Chemie*. 2006;632(8-9):1531–1537.
- [31] Vaqueiro P, Sobany GG. A powder neutron diffraction study of the metallic ferromagnet Co₃Sn₂S₂. *Solid state sciences*. 2009;11(2):513–518.
- [32] Kubodera T, Okabe H, Kamihara Y, Matoba M. Ni substitution effect on magnetic and transport properties in metallic ferromagnet Co₃Sn₂S₂. *Physica B: Condensed Matter*. 2006;378:1142–1143.
- [33] Schnelle W, Leithe-Jasper A, Rosner H, et al. Ferromagnetic ordering and half-metallic state of Sn₂Co₃S₂ with the shandite-type structure. *Physical Review B—Condensed Matter and Materials Physics*. 2013;88(14):144404.
- [34] Liu E, Sun Y, Kumar N, et al. Giant anomalous Hall effect in a ferromagnetic kagome-lattice semimetal. *Nature physics*. 2018;14(11):1125–1131.
- [35] Wang Q, Xu Y, Lou R, et al. Large intrinsic anomalous Hall effect in half-metallic ferromagnet Co₃Sn₂S₂ with magnetic Weyl fermions. *Nature communications*. 2018;9(1):1–8.
- [36] Kassem MA, Tabata Y, Waki T, Nakamura H. Low-field anomalous magnetic phase in the kagome-lattice shandite Co₃Sn₂S₂. *Physical Review B*. 2017;96(1):014429.
- [37] Okamura Y, Minami S, Kato Y, et al. Giant magneto-optical responses in magnetic Weyl semimetal Co₃Sn₂S₂. *Nature communications*. 2020;11(1):4619.
- [38] Lee C, Vir P, Manna K, et al. Observation of a phase transition within the domain walls of ferromagnetic Co₃Sn₂S₂. *Nature communications*. 2022;13(1):3000.
- [39] Shen Z, Zhu X, Ullah RR, Klavins P, Taufour V. Anomalous depinning of magnetic domain walls within the ferromagnetic phase of the Weyl semimetal Co₃Sn₂S₂. *Journal of Physics: Condensed Matter*. 2022;35(4):045802.
- [40] Guguchia Z, Verezhak J, Gawryluk D, et al. Tunable anomalous Hall conductivity through volume-wise magnetic competition in a topological kagome magnet. *Nature communications*. 2020;11(1):559.
- [41] Soh JR, Yi C, Zivkovic I, et al. Magnetic structure of the topological semimetal Co₃Sn₂S₂. *Physical Review B*. 2022;105(9):094435.
- [42] Zhang Q, Zhang Y, Matsuda M, et al. Hidden local symmetry breaking in a kagome-lattice magnetic Weyl semimetal. *Journal of the American Chemical Society*. 2022;144(31):14339–14350.
- [43] Menil C, Leridon B, Cavanna A, et al. Magnetic memory and distinct spin populations in ferromagnetic Co₃Sn₂S₂. *npj Quantum Materials*. 2025;10(1):23.
- [44] Lindemuth J, Dodrill B. Hall effect measurement handbook: a fundamental tool for semiconductor material characterization. *Edited by*. 2020.
- [45] Cornils M, Paul O. Reverse-magnetic-field reciprocity in conductive samples with extended contacts. *Journal of Applied Physics*. 2008;104(2).
- [46] Wang B, Liu Y, Ren P, et al. Large exchange bias after zero-field cooling from an unmagnetized state. *Physical review letters*. 2011;106(7):077203.
- [47] Bufaiçal L, Bittar E. Essential aspects of the spontaneous exchange bias effect. *Journal of Magnetism and Magnetic Materials*. 2024;599:172109.
- [48] Dzyaloshinsky I. A thermodynamic theory of “weak” ferromagnetism of antiferromagnetics. *Journal of Physics and Chemistry of Solids*. 1958;4(4):241–255.
- [49] Moriya T. New mechanism of anisotropic superexchange interaction. *Physical Review Letters*. 1960;4(5):228.
- [50] Fert A, Cros V, Sampaio J. Skyrmions on the track. *Nature nanotechnology*. 2013;8(3):152–156.
- [51] Tokura Y, Seki S. Multiferroics with spiral spin orders. *Advanced materials*. 2010;22(14):1554–1565.
- [52] Parkin S, Yang SH. Memory on the racetrack. *Nature nanotechnology*. 2015;10(3):195–198.
- [53] Nagaosa N, Tokura Y. Topological properties and dynamics of magnetic skyrmions. *Nature nanotechnology*. 2013;8(12):899–911.
- [54] Smidman M, Adroja D, Hillier AD, et al. Neutron scattering and muon spin relaxation measurements of the noncentrosymmetric antiferromagnet CeCoGe₃. *Physical Review B—Condensed Matter and Materials Physics*. 2013;88(13):134416.
- [55] Suárez-Rodríguez M, De Juan F, Souza I, Gobbi M, Casanova F, Hueso LE. Nonlinear transport in noncentrosymmetric systems. *Nature Materials*. 2025:1–14.
- [56] Yasuda K, Wakatsuki R, Morimoto T, et al. Geometric Hall effects in topological insulator heterostructures. *Nature Physics*. 2016;12(6):555–559.

- [57] Liu C, Zang Y, Ruan W, et al. Dimensional crossover-induced topological Hall effect in a magnetic topological insulator. *Physical review letters*. 2017;119(17):176809.
- [58] Ludbrook B, Dubuis G, Puichaud AH, Ruck B, Granville S. Nucleation and annihilation of skyrmions in Mn₂CoAl observed through the topological Hall effect. *Scientific reports*. 2017;7(1):13620.
- [59] Matsuno J, Ogawa N, Yasuda K, et al. Interface-driven topological Hall effect in SrRuO₃-SrIrO₃ bilayer. *Science advances*. 2016;2(7):e1600304.
- [60] Gerber A. Interpretation of experimental evidence of the topological Hall effect. *Physical Review B*. 2018;98(21):214440.
- [61] Tai L, Dai B, Li J, et al. Distinguishing the two-component anomalous Hall effect from the topological Hall effect. *ACS nano*. 2022;16(10):17336–17346.
- [62] Montgomery H. Method for measuring electrical resistivity of anisotropic materials. *Journal of applied physics*. 1971;42(7):2971–2975.
- [63] Dos Santos C, De Campos A, Da Luz M, et al. Procedure for measuring electrical resistivity of anisotropic materials: A revision of the Montgomery method. *Journal of Applied Physics*. 2011;110(8).
- [64] Hall EH, others . On a new action of the magnet on electric currents. *American Journal of Mathematics*. 1879;2(3):287–292.
- [65] Bruno P, Dugaev V, Taillefumier M. Topological Hall effect and Berry phase in magnetic nanostructures. *Physical review letters*. 2004;93(9):096806.
- [66] Tokura Y, Kanazawa N. Magnetic skyrmion materials. *Chemical Reviews*. 2020;121(5):2857–2897.
- [67] Wang H, Dai Y, Chow GM, Chen J. Topological hall transport: Materials, mechanisms and potential applications. *Progress in Materials Science*. 2022;130:100971.
- [68] Kimbell G, Kim C, Wu W, Cuoco M, Robinson JW. Challenges in identifying chiral spin textures via the topological Hall effect. *Communications Materials*. 2022;3(1):19.
- [69] Kurumaji T, Fang S, Ye L, Kitou S, Checkelsky JG. Metamagnetic multiband Hall effect in Ising antiferromagnet ErGa₂. *Proceedings of the National Academy of Sciences*. 2024;121(23):e2318411121.
- [70] Rai B, Kumar N. Cusplike feature in the Hall resistivity of a uniaxial ferromagnet in nonorthogonal Hall geometry. *Physical Review B*. 2025;112(3):035110.
- [71] Parkin S, Friend R. 3 d transition-metal intercalates of the niobium and tantalum dichalcogenides. I. Magnetic properties. *Philosophical Magazine B*. 1980;41(1):65–93.
- [72] Parkin S, Friend R. 3 d transition-metal intercalates of the niobium and tantalum dichalcogenides. II. Transport properties. *Philosophical Magazine B*. 1980;41(1):95–112.
- [73] Parkin S, Friend R. Magnetic and transport properties of 3d transition metal intercalates of some group Va transition metal dichalcogenides. *Physica B+C*. 1980;99(1–4):219–223.
- [74] Miyadai T, Kikuchi K, Kondo H, Sakka S, Arai M, Ishikawa Y. Magnetic Properties of Cr_{1/3}NbS₂. *Journal of the Physical Society of Japan*. 1983;52(4):1394–1401.
- [75] Togawa Y, Koyama T, Takayanagi K, et al. Chiral magnetic soliton lattice on a chiral helimagnet. *Physical review letters*. 2012;108(10):107202.
- [76] Clements EM, Das R, Li L, et al. Critical behavior and macroscopic phase diagram of the monoaxial chiral helimagnet Cr_{1/3}NbS₂. *Scientific reports*. 2017;7(1):6545.
- [77] Zhang C, Zhang J, Liu C, et al. Chiral Helimagnetism and One-Dimensional Magnetic Solitons in a Cr-Intercalated Transition Metal Dichalcogenide. *Advanced Materials*. 2021;33(35):2101131.
- [78] Goodge BH, Gonzalez O, Xie LS, Bediako DK, nair. *ACS nano*. 2023;17(20):19865–19876.
- [79] Park P, Cho W, Kim C, et al. Tetrahedral triple-Q magnetic ordering and large spontaneous Hall conductivity in the metallic triangular antiferromagnet Co_{1/3}TaS₂. *Nature Communications*. 2023;14(1):8346.
- [80] Takagi H, Takagi R, Minami S, et al. Spontaneous topological Hall effect induced by non-coplanar antiferromagnetic order in intercalated van der Waals materials. *Nature Physics*. 2023;19(7):961–968.
- [81] Morosan E, Zandbergen H, Li L, et al. Sharp switching of the magnetization in Fe_{1/4}Ta₂S₂. *Physical Review B—Condensed Matter and Materials Physics*. 2007;75(10):104401.
- [82] Checkelsky J, Lee M, Morosan E, Cava R, Ong N. Anomalous Hall effect and magnetoresistance in the layered ferromagnet Fe_{1/4}Ta₂S₂: The inelastic regime. *Physical Review B—Condensed Matter and Materials Physics*. 2008;77(1):014433.
- [83] Chen CW, Chikara S, Zapf VS, Morosan E. Correlations of crystallographic defects and anisotropy with magnetotransport properties in Fe_xTa₂ single crystals (0.23 ≤ x ≤ 0.35). *Physical Review B*. 2016;94(5):054406.
- [84] Hardy WJ, Chen CW, Marcinkova A, et al. Very large magnetoresistance in Fe_{0.28}Ta₂ single crystals. *Physical Review B*. 2015;91(5):054426.
- [85] Nair NL, Maniv E, John C, Doyle S, Orenstein J, Anaytis JG. Electrical switching in a magnetically intercalated transition metal dichalcogenide. *Nature materials*. 2020;19(2):153–157.
- [86] Wu S, Xu Z, Haley SC, et al. Highly tunable magnetic phases in transition-metal dichalcogenide Fe_{1/3+δ}NbS₂. *Physical Review X*. 2022;12(2):021003.
- [87] Ray MK, Fu M, Chen Y, et al. Zero-field Hall effect emerging from a non-Fermi liquid in a collinear antiferromagnet V_{1/3}NbS₂. *Nature Communications*. 2025;16(1):3532.
- [88] Xie LS, Fender SS, Mollazadeh C, et al. Anomalous Hall effect from inter-superlattice scattering in a noncollinear antiferromagnet. *Nature Communications*. 2025;16(1):5711.
- [89] Kong Z, Kaminsky CJ, Groschner CK, et al. Near room-temperature intrinsic exchange bias in an Fe intercalated ZrSe₂ spin glass. *Journal of the American Chemical Society*. 2023;145(36):20041–20052.
- [90] Lin X, Bud'ko SL, Canfield PC. Development of viable solutions for the synthesis of sulfur bearing single crystals. *Philosophical Magazine*. 2012;92(19–21):2436–2447.
- [91] Austin AJ, Badger J, Ullah R, Shi Y, Klavins P, Taufour V. Growth and Analysis of Single Crystal CeCoGe₃.

SUPPLEMENTARY MATERIALS FOR: MEASURING THE HALL EFFECT IN HYSTERETIC MATERIALS

Jaime M. Moya, Anthony Voyemant, Sudipta Chatterjee, Scott B. Lee, Grigorii Skorupskii, Connor J. Pollak, and Leslie M. Schoop

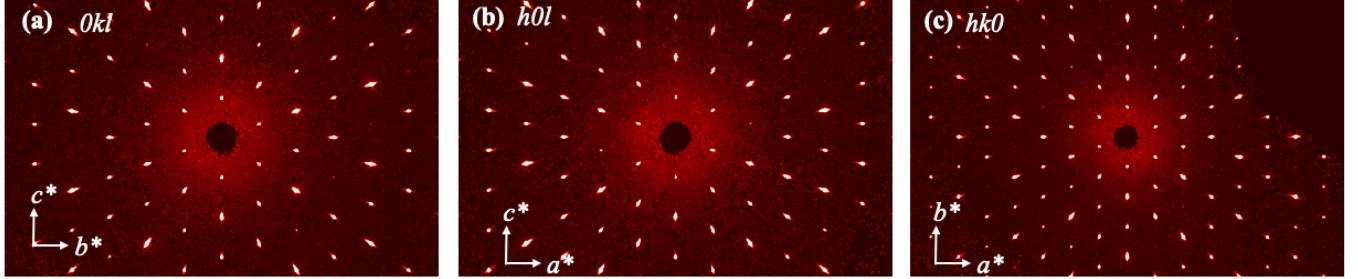


FIG. S1. Precession images of $\text{Co}_3\text{Sn}_2\text{S}_2$ in the (a) $0kl$, (b) $h0l$ and (c) $hk0$ planes measured at 300 K.

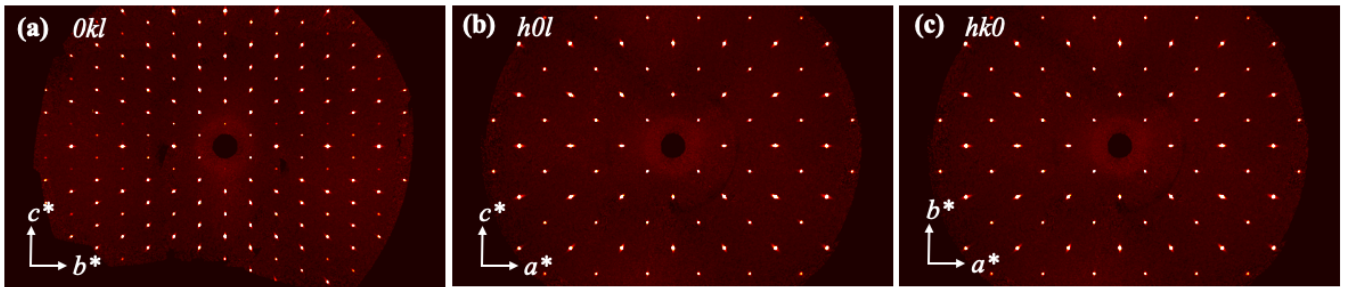


FIG. S2. Precession images of CeCoGe_3 in the (a) $0kl$, (b) $h0l$ and (c) $hk0$ planes measured at 100 K.

Table S S1. Crystallographic Information for $\text{Co}_3\text{Sn}_2\text{S}_2$.

Refined Composition	$\text{Co}_3\text{Sn}_2\text{S}_2$
Crystal Dimension (mm)	$0.084 \times 0.072 \times 0.024$
Radiation Source, λ (Å)	Mo K_α , 0.71073
Absorption Correction	gaussian
Data Collection Temperature (K)	297.84(10)
Space Group	$\text{R}\bar{3}m$
a (Å)	5.36979(10)
c (Å)	13.1835(3)
Cell Volume (Å ³)	329.212(11)
Absorption Coefficient (mm ⁻¹)	23.068
θ_{min} , θ_{max} (deg)	4.64, 44.87
Refinement Method	F^2
$\text{R}_{int}(\text{I} > 3\sigma, \text{all})$	8.43, 8.44
Number of Parameters	13
Unique Reflections ($\text{I} > 3\sigma$, all)	345, 411
$\text{R}(\text{I} > 3\sigma)$, $\text{R}_w(\text{I} > 3\sigma)$	1.48, 4.09
$\text{R}(\text{all})$, $\text{R}_w(\text{all})$	1.54, 4.13
$\text{S}(\text{I} > 3\sigma)$, $\text{S}(\text{all})$	1.2910, 1.2667
$\Delta\rho_{max}$, $\Delta\rho_{min}$ (e Å ⁻³)	0.45, -0.70

Table S S2. Refined atomic coordinates for $\text{Co}_3\text{Sn}_2\text{S}_2$.

Site	Wyckoff Position	x	y	z	Occupancy
Sn1	3a	2/3	1/3	1/3	1
Sn2	3b	1/3	2/3	1/6	1
Co1	9e	1/6	1/3	1/3	1
S1	6c	1/3	2/3	0.44952(5)	1

Table S S3. Refined anisotropic displacement parameters for $\text{Co}_3\text{Sn}_2\text{S}_2$.

Site	U ₁₁	U ₂₂	U ₃₃	U ₁₂	U ₁₃	U ₂₃
Sn1	0.00577(8)	0.00577(8)	0.01288(12)	0.00289(4)	0	0
Sn2	0.00972(9)	0.00972(9)	0.00502(10)	0.00486(4)	0	0
Co1	0.00745(11)	0.00580(13)	0.00752(13)	0.00290(6)	-0.00054(4)	-0.00108(9)
S1	0.00711(17)	0.00711(17)	0.0054(2)	0.00356(8)	0	0

Table S S4. Selected interatomic distances for $\text{Co}_3\text{Sn}_2\text{S}_2$.

Site	Neighbor	Multiplicity	Distance (Å)
Sn1	Co1	6	2.68490(10)
Sn2	Co1	6	2.68901(9)
Co1	S1	2	2.1793(5)

Table S S5. Crystallographic Data for the refinement of CeCoGe_3 .

Refined Composition	CeCoGe ₃	CeCoGe ₃
Crystal Dimension (mm)	$0.062 \times 0.073 \times 0.090$	
Radiation source, λ (Å)		X-ray, 0.7109
Absorption Correction		multi-scan
Data Collection Temperature (K)	100	295
(3+1) D superspace Group		I4mm
<i>a</i> (Å)	4.30949(16)	4.32185(11)
<i>b</i> (Å)	4.30949(16)	4.32185(11)
<i>c</i> (Å)	9.8186(3)	9.8396(2)
Cell Volume (Å ³)	182.348(11)	183.788(8)
Absorption Coefficient (mm ⁻¹)		40.856
$\theta_{min}, \theta_{max}$ (deg)	4.15, 37.73	4.14, 37.9
Refinement Method		F ²
R _{int} (I>3σ, all)	12.49, 12.49	11.42, 11.42
Total Reflections (I >3σ, all)	0, 6071	6229, 6376
Unique Reflections (I >3σ, all)	320, 320	326, 326
Number of Parameters	10	15
R(I>3σ), R _w (I>3σ)	4.55, 11.27	6.06, 13.50
R(all), R _w (all)	4.55, 11.27	6.06, 13.50
S(I>3σ), S(all)	4.7497, 4.7497	5.2155, 5.2155
$\Delta\rho_{max}, \Delta\rho_{min}$ (e Å ⁻³)	1.51, -1.09	2.50, -1.07

Table S S6. **Atomic positions** for the refinement of CeCoGe₃ at 100K.

Label	Element	<i>x</i>	<i>y</i>	<i>z</i>	U_{eq}
Ce1	Ce	0	0	0.43392(8)	0.0006(3)
Ge1	Ge	0.5	0.5	0.5014(2)	0.0012(3)
Ge2	Ge	0.5	0	0.17388(15)	0.0015(3)
Co1	Co	0.5	0.5	0.2680(3)	0.0011(5)

Table S S7. **Atomic positions** for the refinement of CeCoGe₃ at RT.

Label	Element	<i>x</i>	<i>y</i>	<i>z</i>	U_{eq}
Ce1	Ce	0	0	0.53886(11)	0.0072(3)
Ge1	Ge	0.5	0.5	0.4708(2)	0.0072(5)
Ge2	Ge	0.5	0	0.2988(2)	0.0083(5)
Co1	Co	0.5	0.5	0.7042(4)	0.0066(7)

Table S S8. **Components of the anisotropic ADP (U_{ani}) parameters** for the refinement of Crystal CeCoGe₃ 295 K.

Atom	U_{11}	U_{22}	U_{33}	U_{12}	U_{13}	U_{23}
Ce1	0.0071(4)	0.0071(4)	0.0073(6)	0	0	0
Ge1	0.0082(5)	0.0082(5)	0.0051(14)	0	0	0
Ge2	0.0062(9)	0.0121(10)	0.0067(9)	0	0	0
Co1	0.0061(8)	0.0061(8)	0.0074(16)	0	0	0

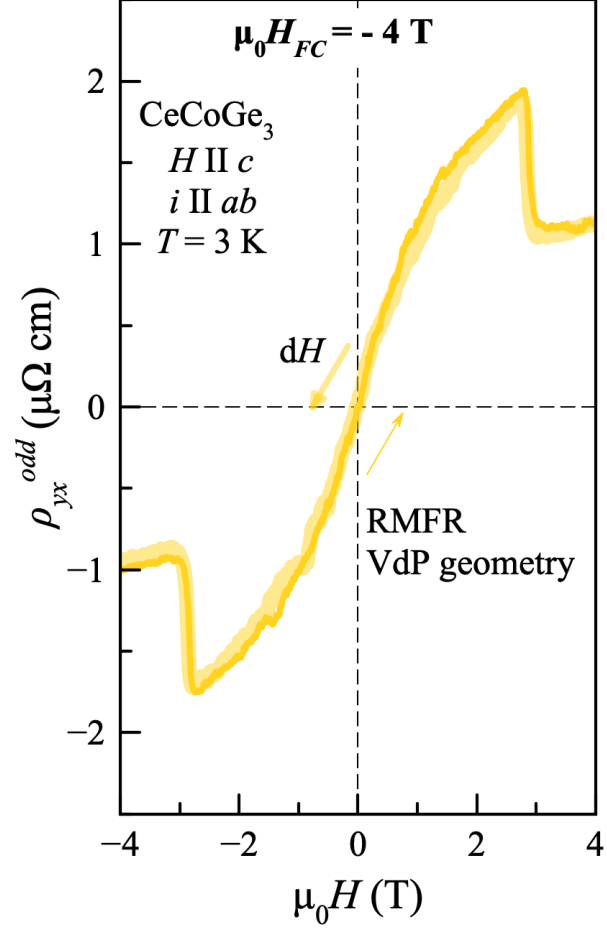


FIG. S3. Isothermal Hall resistivity ρ_{yx}^{odd} of CeCoGe₃ extracted using RMFR in a VdP geometry with Eq. 3 on an independent crystal from the main text measured at temperature $T = 3$ K with magnetic field $H \parallel c$ and current $I \parallel ab$ after field cooling the sample in $\mu_0 H_{FC} = -4$ T.

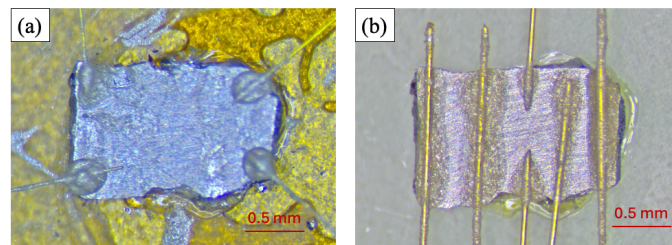


FIG. S4. (a) Van der Pauw and (b) Hall bar geometry used for measuring the Hall effect of Co₃Sn₂S₂.